

1 Multisourced metals enriched by magmatic-hydrothermal
2 fluids in stratabound deposits of the Middle–Lower
3 Yangtze River metallogenic belt, China

4
5 **Yang Li^{1,2,3*}, David Selby^{1,4}, Xian-Hua Li², and Chris J. Ottley¹**

6 *¹Department of Earth Sciences, Durham University, DH1 3LE Durham, UK*

7 *²State Key Laboratory of Lithospheric Evolution, Institute of Geology and Geophysics,
8 Chinese Academy of Sciences, 10029 Beijing, China*

9 *³Department of Geology and Geophysics, Yale University, New Haven, Connecticut
10 06511, CT, USA*

11 *⁴State Key Laboratory of Geological Processes and Mineral Resources, School of Earth
12 Resources, China University of Geosciences, Wuhan, 430074, Hubei, China*

13 *E-mail: yang.li@yale.edu; cugliyang@126.com

14 **ABSTRACT**

15 Stratabound deposits within Late Carboniferous carbonate units in the Middle-
16 Lower Yangtze River metallogenic belt are important Cu producers in China. Hitherto,
17 the genesis of these deposits has been debated, due to poor constraints regarding the
18 timing and source of the mineralization. Proposed models include a Late Carboniferous
19 seafloor exhalative formation (SEDEX), or an Early Cretaceous magmatic-hydrothermal
20 origin. These models imply different metal sources (basinal vs magmatic fluid,
21 respectively) and would require different exploration strategies. New pyrite Re–Os and

22 trace element results from the representative Xinqiao deposit favor a Cretaceous
23 magmatic-hydrothermal genesis over a SEDEX origin. The distinct initial $^{187}\text{Os}/^{188}\text{Os}$
24 compositions (Osi) of different pyrite types (colloform $Osi = 1.4$ and euhedral grains Osi
25 $= 0.7$), coupled with the pyrite trace element abundance, indicate that the Os, and by
26 inference other metals (e.g., Cu, Ag, Au), are sourced from a Cretaceous magmatic-
27 hydrothermal system ($Osi = 0.7$) and Late Permian metalliferous black shales ($Osi = 7.6$
28 ± 3.8). In addition, the genesis of Au-bearing stockwork pyrite veins hosted by the
29 Carboniferous sandstone is best explained by the leaching of existing mineralization (e.g.,
30 porphyry Au-Mo) by Early Cretaceous magmatic-hydrothermal fluids. This is implied by
31 the lack of common Os, high Re abundances (0.6–3.7 ppm), and highly variable Re–Os
32 model ages (379 and 173 Ma), which are positively correlated with Re and total
33 abundances of Co, Ni, Ag, Au, Tl and Ba. This study highlights the importance of
34 recycling multi-sourced metals (sedimentary and existing mineralization) in the
35 formation of intrusion-related stratabound deposits. Furthermore, it demonstrates the
36 importance of integrating information regarding the source and timing of deposit
37 formation within a well-defined geological framework, which can yield information
38 about the ore-forming process and help to guide mineral exploration.

39

40 INTRODUCTION

41 Intrusion-related stratabound deposits, together with porphyry, skarn, and
42 epithermal deposits, are important end-members of porphyry copper systems that
43 contribute significantly to the world's supply of Cu, Mo Au, and other metals (Sillitoe,
44 2010). The presence of non-magmatic fluids in porphyry copper systems, i.e., meteoric

45 and metamorphic fluids, has been ubiquitously documented (D'Errico et al., 2012; Fekete
46 et al., 2016; Li et al., 2017a), but the current consensus is that the metals are derived from
47 magmatic-hydrothermal systems. However, the close spatial association between
48 metalliferous sedimentary rocks and many intrusion-related stratabound deposits raises
49 the possibility that, in addition to magmatic-hydrothermal systems, metal-bearing strata
50 could be a complementary origin of metals.

51 The expansive distribution of intrusion-related stratabound deposits in the
52 Middle–Lower Yangtze River metallogenic belt (Fig. 1A) offers an excellent opportunity
53 to examine the sources of their metals. These deposits comprise predominantly massive
54 ores of chalcopyrite and pyrite, with quartz-Au-bearing pyrite vein stockworks. A unique
55 feature of these stratabound deposits is the ubiquitous presence of colloform pyrite (Gu et
56 al., 2007), and their close spatial association with Early Cretaceous magmatic-porphry-
57 skarn systems (Fig. 1). Although extensively studied, the genesis of these stratabound
58 deposits remains ambiguous, with two principal genetic models having been proposed: 1)
59 linkage to Early Cretaceous porphyry-skarn systems (Pan and Dong, 1999; Mao et al.,
60 2011; Pirajno and Zhou, 2015); and 2) initial formation as a Late Carboniferous SEDEX
61 system, which was then enriched/overprinted by an Early Cretaceous magmatic-
62 hydrothermal event (Zeng et al., 2002; Gu et al., 2007). The contrasting genetic models
63 imply different metal enrichment mechanisms and alternate mineral exploration
64 programs. For example, an Early Cretaceous magmatic-hydrothermal origin suggests that
65 these deposits are similar to manto-type deposits (Mao et al., 2011; Li et al., 2017b;
66 Zhang et al., 2017) in Mexico and Chile (Meinert, 1982; Sato, 1984). Therefore, a
67 magmatic origin of metals is most likely, with stratabound deposits being expected to

68 center around Cretaceous granites. On the other hand, a Carboniferous SEDEX origin
69 (Xu and Zhou, 2001; Zeng et al., 2002; Gu et al., 2007; Guo et al., 2011; Xie et al., 2014)
70 would suggest that the metals were sourced from the underlying strata by a migrating
71 basinal fluid, and therefore the stratabound mineralization could be more laterally
72 extensive within the Late Carboniferous limestone.

73 Uncertainty regarding ore genesis in the Middle–Lower Yangtze River
74 metallogenic belt is primarily due to the lack of constraint on the timing of mineralization
75 and a poor understanding of the source of the metals, which is a typical challenge for
76 hydrothermal deposit studies. Here, based on a robust geological framework, the
77 representative Xinqiao deposit of the Middle–Lower Yangtze River metallogenic belt is
78 selected for a pyrite Re–Os and trace element study, in order to provide an improved
79 genetic understanding and yield implications for mineral exploration.

80 **STRATABOUND DEPOSITS OF THE MIDDLE–LOWER YANGTZE RIVER** 81 **METALLOGENIC BELT**

82 As represented by Xinqiao, stratabound ore bodies in the Middle–Lower
83 Yangtze River metallogenic belt are hosted primarily by limestone and dolomite units
84 within the Late–Middle Carboniferous Chuanshan–Huanglong formations. These units lie
85 above the Early Carboniferous Gaolishan Formation sandstone (Figs. 1B and 1C). Minor
86 massive pyritic ores are also present in overlying Permian and Triassic carbonate units.
87 The deposits exhibit a close spatial association with Early Cretaceous (ca. 135–145 Ma)
88 granitoids (Zhou et al., 2008; Li et al., 2010), which are hosted by Carboniferous–
89 Permian carbonate units. Many of the granitoids are associated with porphyry and skarn
90 mineralization (Mao et al., 2011; Pirajno and Zhou, 2015). The stratabound ore bodies

91 predominantly comprise Cu-bearing pyrite and pyrrhotite (Li et al., 2017b). Unique to
92 these deposits is pyrite exhibiting a colloform texture (Xie et al., 2014). In most cases, no
93 direct contact relationship is observed between the colloform ore and sedimentary rocks,
94 but veins bearing colloform pyrite are observed to locally cross-cut the Permian
95 limestone (Fig. DR3). Vertical to sub-vertical Au-bearing pyrite stockworks occur
96 beneath the stratabound ore bodies hosted by the Early Carboniferous Gaolishan
97 Formation sandstone (Guo et al., 2011; Zhang et al., 2017).

98 **PYRITE RE–OS AND TRACE ELEMENT RESULTS**

99 Four styles of pyritic mineralization (Figs. 1 and 2) from Xinqiao were examined
100 for Re–Os and trace element analysis. Deposit geology, sample details, analytical
101 methods, and pyrite Re–Os and trace element data are presented in the GSA data
102 repository. Euhedral pyrite grains (py1) from the stratabound ore body have Re and ^{192}Os
103 concentrations of 1.5–3.6 ppb and 1.7–4.0 ppt, respectively, and yield a Re–Os isochron
104 age of 135.5 ± 4.0 Ma (initial $^{187}\text{Os}/^{188}\text{Os}$ composition (Os_i) = 0.79 ± 0.11 ; $n = 5$; MSWD
105 = 2.2; Fig. 2E). Colloform pyrite (py2) from the stratabound ore body possesses 1.2–9.3
106 ppb Re and 2.0–43.4 ppt ^{192}Os , and yields a Re–Os isochron age of 136.6 ± 4.6 Ma (Os_i
107 = 1.35 ± 0.06 ; $n = 11$; MSWD = 5.4; Fig. 2E). Euhedral garnet-skarn pyrite (py3)
108 contains 1.4–1.6 ppb Re and 1.4–2.1 ppt ^{192}Os . For py3, although only two samples
109 (XQ15-5-3 and XQ15-5-4) were analyzed, which is not sufficient to yield a statistically
110 valid isochron, the Re–Os data yield an errorchron with a date of 143 ± 16 Ma and an Os_i
111 of 0.63 ± 0.44 (Fig. 2E). The sandstone-hosted pyrites (py4) possess 57–3692 ppb Re,
112 1.3–43.1 ppt ^{192}Os , and negligible common Os (< 0.45%, Table DR1). The model ^{187}Re –
113 ^{187}Os ages of these pyrite grains range from 173.2 ± 1.7 – 359.0 ± 1.8 Ma (Fig. 2F).

114 Overall, Py1 and Py3 are characterized by low trace element abundance, but contain
115 moderate Mn, Cu, Pb, Zn, W, and Ag (Table DR2). Py2 has higher abundances of Mn,
116 Sb, Cu, Pb, Zn and Ag; py4 enriched in Au, Ba, Co, Ni and Tl (Fig. 3A). For py4, a
117 positive correlation is observed between the total abundances of Co, Ni, Ag, Au, Tl, Ba,
118 Re and Re–Os model ages (Fig. 3B).

119 **DISCUSSION AND IMPLICATIONS**

120 **Magmatic and Sedimentary Sourced Metals for Stratabound Ore**

121 The Re–Os ages of py1 and py2 (135.5 ± 4.0 and 136.7 ± 4.6 Ma; Fig. 2E)
122 suggest that the two types of mineralization (euhedral and colloform pyrite) were formed
123 broadly contemporaneously, and are indistinguishable from the emplacement age of the
124 Jitou Stock (138.5 ± 1.0 Ma; Li et al., 2017b) at Xinqiao. In addition, these ages overlap
125 with the Re–Os age of the skarn pyrite, py3 (143 ± 16 Ma; Fig. 2E). Thus, a temporal link
126 exists between the Early Cretaceous magmatic-skarn system associated with the Jitou
127 Stock and the stratabound mineralization. This is inconsistent with a Carboniferous
128 SEDEX origin (Xu and Zhou, 2001; Zeng et al., 2002; Xie et al., 2014).

129 At the time of emplacement of the Jitou Stock (138.5 ± 1.0 Ma), the skarn pyrite
130 (py3) had an Osi of 0.74 ± 0.24 . Taking this value as the maximum estimate of the
131 magmatic Osi , a crust-derived origin with limited mantle input ($Osi = 0.13$) is inferred for
132 the Jitou Stock. This is consistent with Jitou Stock zircon depleted Hf isotope
133 composition ($\epsilon_{Hf} = \sim -11$; Zhang et al., 2017). The similar Osi values (0.79 ± 0.11 vs 0.74
134 ± 0.24) for py1 and py3 imply that the Os, and by inference the associated metals, were
135 predominantly sourced from the Early Cretaceous magmatic-hydrothermal system.

136 It has been previously proposed that the colloform pyrite was initially formed in
137 the Carboniferous (Xu and Zhou, 2001; Zeng et al., 2002; Gu et al., 2007; Xie et al.,
138 2014), and then recrystallized to euhedral pyrite during the Early Cretaceous magmatic-
139 hydrothermal event. This scenario is not supported by the sharp contact relationship
140 between the euhedral and colloform pyrites (Fig. DR2A), nor by the cross-cutting
141 relationship between the colloform pyrite and Permian limestones at Dongguashan and
142 Wushan (Fig. DR3). In addition, the *Osi* (Fig. 2E) and trace element abundances (Figs.
143 3A and 3B) of py2 are distinct from py1, hence a recrystallization origin of py1 from py2
144 is unlikely. Further, the colloform pyrite is composed of fine-grained (80 nm–1.5 μm)
145 cubic crystals and not framboids, which is inconsistent with a sedimentary origin
146 (Sweeney and Kaplan, 1973). Moreover, *in-situ* sulfur isotope data for the four types of
147 pyrite studied here have indistinguishable $\delta^{34}\text{S}$ values (0–4 ‰). All of these data support
148 a magmatic-hydrothermal origin rather than a SEDEX genesis (Zhang et al., 2017).

149 The highly radiogenic *Osi* (1.35 ± 0.06) of the colloform pyrite indicates that the
150 *Osi* and by inference the metals are not solely magmatically derived. In the Xinqiao area,
151 the most likely source to provide a radiogenic $^{187}\text{Os}/^{188}\text{Os}$ composition is the Late
152 Permian metalliferous black shales. These shales are enriched in Re (403 – 1002 ppb) and
153 Os (0.3 – 1 ppb) and yield an Early Cretaceous $^{187}\text{Os}/^{188}\text{Os}$ composition of 7.6 ± 3.8
154 (Yang et al., 2004). Therefore, the most geological plausible scenario is that the
155 colloform pyrite was formed through intensive water-rock interaction between the Early
156 Cretaceous magmatic-hydrothermal fluids and the Late Permian metalliferous black
157 shales.

158 **Cycling Existing Mineralization for the Au-Bearing Pyrite Stockworks**

159 The Au-bearing pyrite (py4) veins hosted by the sandstone underlying the
160 stratabound ore body are dated at 138 ± 2.3 Ma (quartz fluid inclusion Rb–Sr; initial
161 $^{87}\text{Sr}/^{86}\text{Sr} = 0.71138 \pm 0.00014$; Zhang et al., 2017), suggesting a temporal and genetic
162 association with the Jitou Stock, which is further supported by fluid inclusion and $\delta^{18}\text{O}$
163 data from quartz co-precipitated with py4 (up to 597 °C and 63.7 % NaCl equiv.; $6.81 \pm$
164 2.76 ‰; Wang and Ni, 2009; Li et al., 2017b). In contrast, a 319 ± 13 Ma Re–Os age ($n =$
165 9 ; MSWD = 13; Guo et al., 2011) for py4 seems consistent with the hypothesis that these
166 pyrite veins were the fluid conduit (stockwork feeder) for a Carboniferous SEDEX
167 system (Xu and Zhou, 2001; Zeng et al., 2002; Gu et al., 2007). However, a SEDEX
168 scenario is not supported by the following observations. First, py4 Re–Os data from both
169 this study and Guo et al. (2011) share similar characteristics (enriched in Re and limited
170 to no common Os) and yield highly variable model ages (173–379 Ma). Therefore, the
171 py4 Re–Os data do not meet the necessary criteria for isochron dating. Second, py4 does
172 not contain common Os, but in SEDEX systems, the basinal fluid must interact with the
173 basement rocks, and hence should inherit common Os with a radiogenic O_{si} (Hnatyshin
174 et al., 2015). Third, the pyrite veins beneath the stratabound ore body are structurally
175 controlled and only possess silicified and sericite-bearing selvages (Wang and Ni, 2009;
176 Guo et al., 2011; Li et al., 2017b). In contrast, the fluid conduits in SEDEX systems are
177 developed in syn-sedimentary faults and are characterized by tourmaline- and albite-
178 bearing alteration assemblages (Leach et al., 2005). As such, in accordance with the 138
179 ± 2.3 Ma Rb–Sr age (Zhang et al., 2017), we suggest that the sandstone-hosted
180 mineralization was temporally associated with the Early Cretaceous magmatic-
181 hydrothermal system.

182 For py4, in order to yield geologically reasonable ages (ca 138 Ma), each sample
183 has to be corrected using widely different and geologically implausible O_{Si} (e.g., -223–
184 59; Table DR1). Given the fact that these samples possess very high abundances of Re
185 and radiogenic Os with negligible common Os, it is unlikely that the observed ages are
186 caused by disturbance of the Re–Os systematics. In this regard, the most plausible
187 genesis for py4 is the leaching of rocks enriched in Re and radiogenic Os by the Early
188 Cretaceous magmatic-hydrothermal fluid. A higher degree of water-rock interaction
189 resulted in the inheritance of more Re, ^{187}Os and trace elements, which is consistent with
190 the positive correlations between model ages of py4 and their Re and trace element
191 concentrations (Figs. 2F, 3A and 3B). Rhenium and Os concentrations are typically very
192 low in crustal rocks (0.20 and 0.03 ppb, respectively), but are known to be high in
193 molybdenite (e.g., hundreds to thousands ppm for Re and ppm level for ^{187}Os) and to a
194 lesser extent in other sulfides, such as chalcocite, chalcopyrite, bornite, and pyrite (Selby
195 et al., 2009; Stein, 2014). As such, the most likely source for the elevated Re (ppm level),
196 radiogenic Os (^{187}Os , ppb level), and negligible common Os in py4 is porphyry-style Au-
197 Mo mineralization.

198 **Implications for Ore Genesis and Metals Origin**

199 In the Middle–Lower Yangtze River metallogenic belt, stratabound deposits are
200 all spatially associated with the Early Cretaceous magmatic-porphyry-skarn systems (Fig.
201 1A), and the ore-forming fluids and alteration assemblages have a close magmatic
202 affinity, but barely show characteristics of typical SEDEX systems (Pan and Dong, 1999;
203 Mao et al., 2011). As such, an Early Cretaceous intrusion-related carbonate replacement
204 origin is suggested, with the stratabound orebodies being spatially controlled by the

205 unconformity between the Early Carboniferous sandstone and Late Carboniferous
206 carbonate units, and the Au-bearing stockworks being a product of recycled pre-existing
207 porphyry-style mineralization by the Early Cretaceous magmatic-hydrothermal fluid (Fig.
208 4).

209 This study highlights that coupling absolute timing and source constraints for
210 mineralization with a detailed geological framework can significantly advance our
211 understanding of the ore-forming process of intrusion-related stratabound deposits, and
212 underpin exploration models. Further, the recycling of metals from metalliferous
213 sedimentary rocks (i.e., black shales) and pre-existing mineralization by magmatic-
214 hydrothermal fluids could be an important mechanism for the formation of ore deposits.

215 **ACKNOWLEDGMENTS**

216 YL acknowledges a 2-month fellowship and a grant (SKL-K201706) from IGG-
217 CAS, and extends his gratitude to Jian-Wei Li for his encouragement during this study.
218 DS acknowledges the Total endowment fund and Dida scholarship (CUG Wuhan). We
219 thank Zhen-Ting Jiang for assistance with SEM imaging, and Ann Bauer, Alan Rooney
220 and Rachael Bullock for editorial comments, and extend our thanks to the editor and
221 reviewers of Geology for their constructive and insightful comments.

222 **REFERENCES CITED**

223 D'Errico, M.E., Lackey, J.S., Surpless, B.E., Loewy, S.L., Wooden, J.L., Barnes, J.D.,
224 Strickland, A., and Valley, J.W., 2012, A detailed record of shallow hydrothermal
225 fluid flow in the Sierra Nevada magmatic arc from low- $\delta^{18}\text{O}$ skarn garnets: Geology,
226 v. 40, p. 763–766, <https://doi.org/10.1130/G33008.1>.

- 227 Fekete, S., Weis, P., Driesner, T., Bouvier, A.S., Baumgartner, L., and Heinrich, C.A.,
228 2016, Contrasting hydrological processes of meteoric water incursion during
229 magmatic-hydrothermal ore deposition: An oxygen isotope study by ion microprobe:
230 Earth and Planetary Science Letters, v. 451, p. 263–271,
231 <https://doi.org/10.1016/j.epsl.2016.07.009>.
- 232 Gu, L.X., Zaw, K., Hu, W.X., Zhang, K.J., Ni, P., He, J.X., Xu, Y.T., Lu, J.J., and Lin,
233 C.M., 2007, Distinctive features of Late Palaeozoic massive sulphide deposits in
234 South China: Ore Geology Reviews, v. 31, p. 107–138,
235 <https://doi.org/10.1016/j.oregeorev.2005.01.002>.
- 236 Guo, W.M., Lu, J.J., Jiang, S.Y., Zhang, R.Q., and Qi, L., 2011, Re-Os isotope dating of
237 pyrite from the footwall mineralization zone of the Xinqiao deposit, Tongling, Anhui
238 Province: Geochronological evidence for submarine exhalative sedimentation:
239 Chinese Science Bulletin, v. 56, p. 3860–3865, [https://doi.org/10.1007/s11434-011-](https://doi.org/10.1007/s11434-011-4770-y)
240 [4770-y](https://doi.org/10.1007/s11434-011-4770-y).
- 241 Hnatyshin, D., Creaser, R.A., Wilkinson, J.J., and Gleeson, S.A., 2015, Re-Os dating of
242 pyrite confirms an early diagenetic onset and extended duration of mineralization in
243 the Irish Zn-Pb ore field: Geology, v. 43, p. 143–146,
244 <https://doi.org/10.1130/G36296.1>.
- 245 Leach, D., Sangster, D., Kelley, K., Large, R., Garven, G., Allen, C., Gutzmer, J., and
246 Walters, S.G., 2005, Sediment-hosted lead-zinc deposits: A global perspective:
247 Economic Geology and the Bulletin of the Society of Economic Geologists, v. 100,
248 p. 561–607.

- 249 Li, X.H., Li, W.X., Wang, X.C., Li, Q.L., Liu, Y., Tang, G.Q., Gao, Y.Y., and Wu, F.Y.,
250 2010, SIMS U-Pb zircon geochronology of porphyry Cu-Au-(Mo) deposits in the
251 Yangtze River Metallogenic Belt, eastern China: Magmatic response to early
252 Cretaceous lithospheric extension: *Lithos*, v. 119, p. 427–438,
253 <https://doi.org/10.1016/j.lithos.2010.07.018>.
- 254 Li, Y., Li, X. H., Selby, D., and Li, J. W., 2017a, Pulsed magmatic fluid release for the
255 formation of porphyry deposits: tracing fluid evolution in absolute-time from the
256 Tibetan Qulong Cu-Mo deposit: *Geology*, v. 46, no. 1, p. 7-11,
257 <https://doi:10.1130/G39504.1>.
- 258 Li, Y., Li, J.W., Li, X.H., Selby, D., Huang, G.H., Chen, L.J., and Zheng, K., 2017b, An
259 Early Cretaceous carbonate replacement origin for the Xinqiao stratabound massive
260 sulfide deposit, Middle-Lower Yangtze Metallogenic Belt, China: *Ore Geology*
261 *Reviews*, v. 80, p. 985–1003, <https://doi.org/10.1016/j.oregeorev.2016.08.017>.
- 262 Mao, J.W., Xie, G.Q., Duan, C., Pirajno, F., Ishiyama, D., and Chen, Y.C., 2011, A
263 tectono-genetic model for porphyry-skarn-stratabound Cu-Au-Mo-Fe and magnetite-
264 apatite deposits along the Middle-Lower Yangtze River Valley, Eastern China: *Ore*
265 *Geology Reviews*, v. 43, p. 294–314,
266 <https://doi.org/10.1016/j.oregeorev.2011.07.010>.
- 267 Meinert, L.D., 1982, Skarn, Manto, and Breccia Pipe Formation in Sedimentary-Rocks of
268 the Cananea Mining District, Sonora, Mexico: *Economic Geology and the Bulletin*
269 *of the Society of Economic Geologists*, v. 77, p. 919–949,
270 <https://doi.org/10.2113/gsecongeo.77.4.919>.

- 271 Pan, Y.M., and Dong, P., 1999, The Lower Changjiang (Yangzi/Yangtze River)
272 metallogenic belt, east central China: Intrusion- and wall rock-hosted Cu-Fe-Au, Mo,
273 Zn, Pb, Ag deposits: *Ore Geology Reviews*, v. 15, p. 177–242,
274 [https://doi.org/10.1016/S0169-1368\(99\)00022-0](https://doi.org/10.1016/S0169-1368(99)00022-0).
- 275 Pirajno, F., and Zhou, T., 2015, Intracontinental Porphyry and Porphyry-Skarn Mineral
276 Systems in Eastern China: Scrutiny of a Special Case “Made-in-China”: *Economic
277 Geology and the Bulletin of the Society of Economic Geologists*, v. 110, p. 603–629,
278 <https://doi.org/10.2113/econgeo.110.3.603>.
- 279 Sato, T., 1984, Manto type copper deposits in Chile: A review: *Bulletin of the Geological
280 Survey of Japan*, v. 35, p. 565–582.
- 281 Selby, D., Kelley, K.D., Hitzman, M.W., and Zieg, J., 2009, Re-Os sulfide (bornite,
282 chalcopyrite, and pyrite) systematics of the carbonate-hosted copper deposits at Ruby
283 Creek, southern Brooks Range, Alaska: *Economic Geology and the Bulletin of the
284 Society of Economic Geologists*, v. 104, p. 437–444,
285 <https://doi.org/10.2113/gsecongeo.104.3.437>.
- 286 Sillitoe, R.H., 2010, Porphyry Copper Systems: *Economic Geology and the Bulletin of
287 the Society of Economic Geologists*, v. 105, p. 3–41,
288 <https://doi.org/10.2113/gsecongeo.105.1.3>.
- 289 Sweeney, R. E., and Kaplan, I. R., 1973, Pyrite Framboid Formation; Laboratory
290 Synthesis and Marine Sediments: *Economic Geology*, v. 68, no. 5, p. 618-634.
291 <https://doi.org/10.2113/gsecongeo.68.5.618>

- 292 Stein, H.J., 2014, Dating and Tracing the History of Ore Formation, *in* Turekian, H. D. H.
293 K., ed., *Treatise on Geochemistry (Second Edition)*: Oxford, Elsevier, p. 87–118,
294 <https://doi.org/10.1016/B978-0-08-095975-7.01104-9>.
- 295 Wang, G.-G., and Ni, P., 2009, Fluid inclusions study for the pyrite vein beneath Xinqiao
296 stritiform massive Cu deposit [in Chinese]: *Acta Mineralogica Sinica*, v. 29, p. 256.
- 297 Xie, Q.-Q., Chen, T.-H., Fan, Z.-L., Xu, X.-C., Zhou, Y.-F., Shi, W.-B., and Xue, J.-J.,
298 2014, Morphological characteristics and genesis of colloform pyrite in Xinqiao Fe-S
299 deposit, Tongling, Anhui Province [in Chinese]: *Scientia Sinica Terrae*, v. 44,
300 p. 2665–2674.
- 301 Xu, G., and Zhou, J., 2001, The Xinqiao Cu-S-Fe-Au deposit in the Tongling mineral
302 district, China: Synorogenic remobilization of a stratiform sulfide deposit: *Ore*
303 *Geology Reviews*, v. 18, p. 77–94, [https://doi.org/10.1016/S0169-1368\(01\)00017-8](https://doi.org/10.1016/S0169-1368(01)00017-8).
- 304 Yang, G., Chen, J.F., Du, A.D., Qu, W.J., and Yu, G., 2004, Re-Os dating of the Mo-
305 bearing black shale from Laoyalong, Anhui [in Chinese]: *Chinese Science Bulletin*,
306 v. 49, p. 1205–1208.
- 307 Zeng, P.-S., Pei, R.-F., and Hou, Z.-Q., 2002, Sedex-type massive sulfide deposits in
308 Tongling Block, Anhui [in Chinese]: *Mineralium Deposita*, v. 21, p. 532–535.
- 309 Zhang, Y., Shao, Y.J., Li, H.B., and Liu, Z.F., 2017, Genesis of the Xinqiao Cu-S-Fe-Au
310 deposit in the Middle-Lower Yangtze River Valley metallogenic belt, Eastern China:
311 Constraints from U-Pb-Hf, Rb-Sr, S, and Pb isotopes: *Ore Geology Reviews*, v. 86,
312 p. 100–116, <https://doi.org/10.1016/j.oregeorev.2017.02.014>.

313 Zhou, T.F., Yu, F., and Yuan, F., 2008, Advances on petrogenesis and metallogeny study
314 of the mineralization belt of the Middle and Lower Reaches of the Yangtze River
315 area [in Chinese with English abstract]: *Yanshi Xuebao*, v. 24, p. 1665–1678.

316

317 **FIGURE CAPTIONS**

318

319 Figure 1. A), Distribution of porphyry-skarn and stratabound deposits in the Middle–
320 Lower Yangtze River metallogenic belt and their spatial association with Early
321 Cretaceous granites. Modified after Pan and Dong (1999) and Mao et al. (2011). B),
322 Geological map of the Xinqiao stratabound ore deposit. C), Cross section of the Xinqiao
323 deposit and relevant chronological data. 1, Li et al. (2017b); 2, Yang et al. (2004); 3, this
324 study; 4, Guo et al. (2011); 5, Zhang et al. (2017).

325

326 Figure 2. Representative pyrite mineralization at Xinqiao and their Re–Os ages. A),
327 Euhedral pyrite grains (py1) cemented by calcite from the stratabound ore body. B),
328 Colloform pyrite (py2) from the stratabound ore body, which is composed of fine-grained
329 (80 nm–1.5 μm) cubic pyrite grains, with local distribution of calcite grains. No
330 framboidal pyrite grains are observed in this study. C), Pyrite samples (py3) from the
331 garnet-bearing skarn ore. D), Pyrite samples (py4) hosted by sandstone beneath the
332 stratabound ore body. E), Re–Os isochrons of py1, py2 and py3. F), Model ages of py4
333 and their correlation with Re abundances. Also shown are data from Guo et al. (2011). Py
334 = pyrite, cal = calcite, qtz = quartz, gar = garnet. Resin refers to the materials used for

335 making mounts. MSWD = Mean Squared Weighted Deviation. All uncertainties are at
336 the 2-sigma level.

337

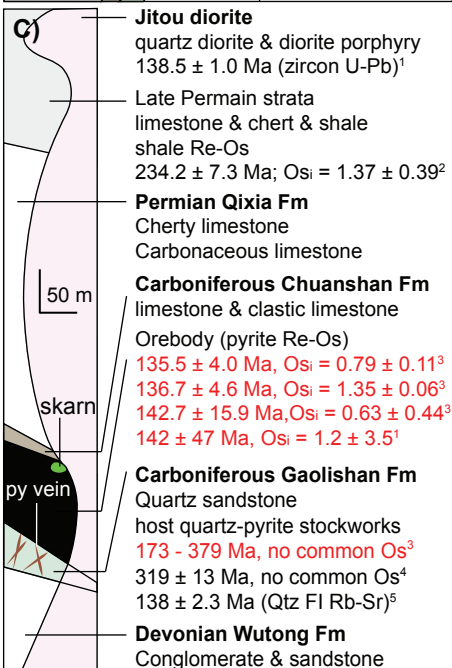
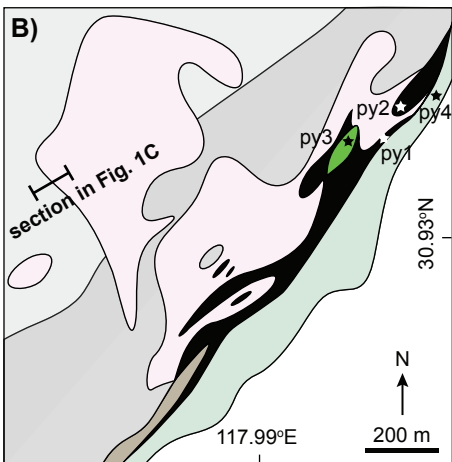
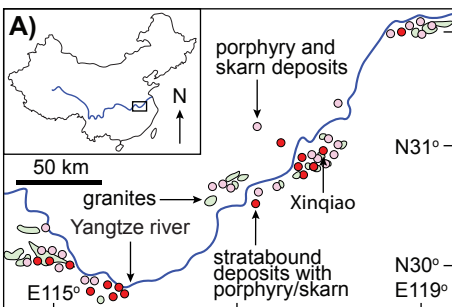
338 Figure 3. Trace element compositions of the studied pyrite samples. A), Py2 is
339 characterized by high total abundances of Co, Ni, Ag, Au, Tl, Ba; py4 is enriched in Cu,
340 W, Pb, Zn. In contrast, py1 and py3 are depleted in these trace elements. B), The model
341 ages of py4 are positively correlated with their total abundances of Co, Ni, Ag, Au, Tl
342 and Ba. Uncertainties are smaller than the symbol size.

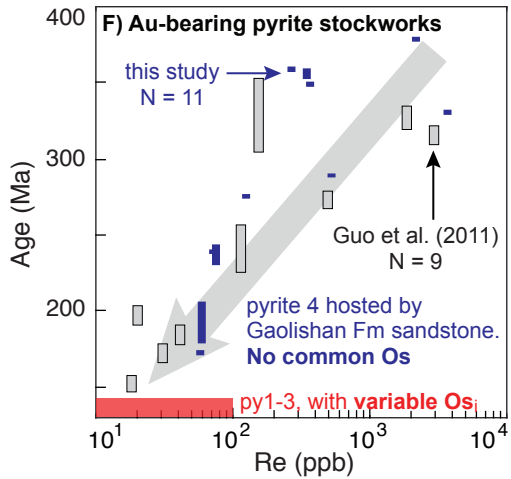
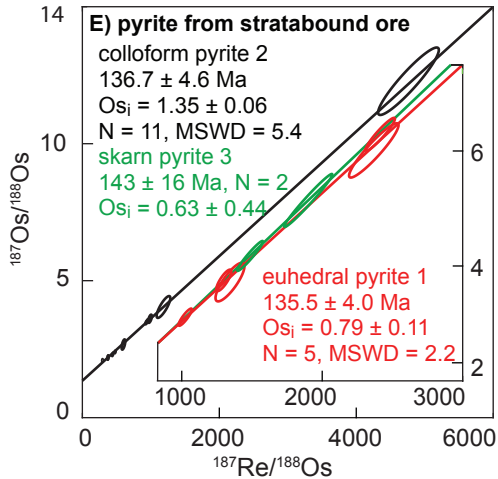
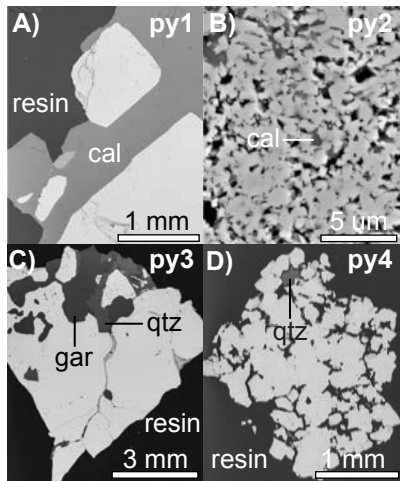
343

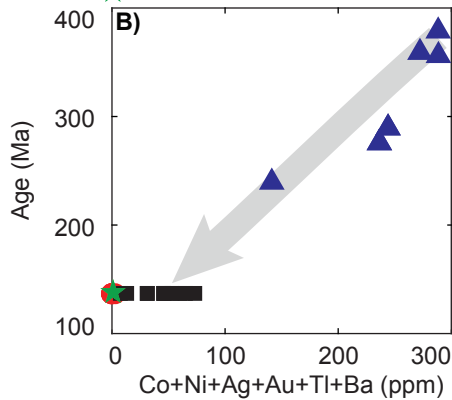
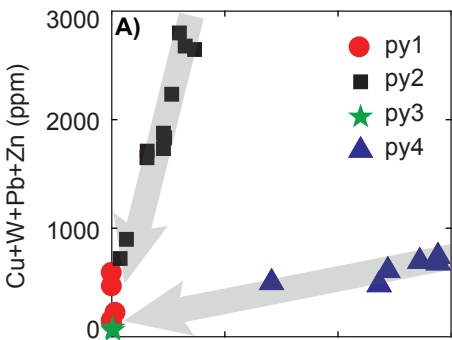
344 Figure 4. Sketch illustrating the genesis of intrusion-related stratabound deposits in the
345 Middle–Lower Yangtze metallogenic belt, which is temporally and spatially associated
346 with Early Cretaceous granites, porphyry and skarn deposits. The model highlights the
347 importance of recycling metals from metalliferous sedimentary rocks and pre-existing
348 mineralization in the formation of intrusion-related stratabound deposits.

349

350 1GSA Data Repository item 2018xxx, Deposit geology, samples, analytical methods,
351 Pyrite Re-Os and trace elements data, is available online at
352 <http://www.geosociety.org/datarepository/2018/> or on request from
353 editing@geosociety.org.







black shales

limestone

stratabound ore

fault

py veins in sandstone

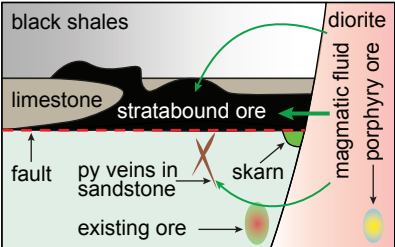
existing ore

skarn

diorite

magmatic fluid

porphyry ore



Data Repository for

Multisourced metals enriched by magmatic-hydrothermal fluid in
stratabound deposits of the Middle-Lower Yangtze River
metallogenic belt, China

Yang Li^{1,2,3*}, David Selby^{1,4}, Xian-Hua Li², and Chris J. Ottley¹

¹Department of Earth Sciences, Durham University, DH1 3LE Durham, UK

²State Key Laboratory of Lithospheric Evolution, Institute of Geology and Geophysics, Chinese Academy of Sciences, 10029 Beijing, China

³Department of Geology and Geophysics, Yale University, New Haven, Connecticut 06511, CT, USA

⁴State Key Laboratory of Geological Processes and Mineral Resources, School of Earth Resources, China University of Geosciences, Wuhan, 430074, Hubei, China

*E-mail: yang.li@yale.edu; cugliyang@126.com

A1. Deposit Geology, Sample location and details

At the Xinqiao deposit, the stratabound ore body (Fig. DR1) strikes NE-SW and dips ($\sim 45^\circ$) northwest, with horizontal and vertical extensions and an average thickness of 2550 m, 1810 m, and 21 m, respectively (Xu and Zhou, 2001). The stratabound ore body (Fig. DR2A) predominantly comprises Cu-bearing massive euhedral pyrite (py1, Figure 2A and DR2B) and colloform pyrite (py2, Figure 2B and DR2C), although massive chalcopyrite and anhedral pyrite are also present. The Jitou diorite (SIMS U-Pb zircon age of $\sim 138.5 \pm 1.0$ Ma; Li et al., 2017) was emplaced into the Carboniferous-Permian carbonate units, which is associated with intense skarn garnet-diopside-epidote alteration (Zhang et al., 2017), that is crosscut by ~ 1 cm wide pyrite \pm chalcopyrite veins (py3, Figures 2C and DR2D). Beneath the stratabound ore body, the Gaolishan Formation sandstone is extensively fractured (Fig. DR2E), and hosts vertical to sub-vertical Au-bearing pyrite stockworks (py4, Fig. 2D) with $\sim 1 - 10$ cm wide silicified and sericite-bearing selvages (Guo et al., 2011).

Sample locations are illustrated in Figure 1B and Figure DR3. In Figure DR3, the portion that has been removed/mined is the stratabound ore body. All samples were collected from the outcrops in the open pit. Euhedral pyrite (XQ15-9, py1) and colloform pyrite (XQ15-4, py2) samples of the stratabound orebody were collected from fresh outcrop (Fig. DR1, DR1A) exposed during the mining process. The outcrop is located in the southwest wall of the open pit, where the colloform pyrite ore and euhedral pyrite ore have a sharp contact relationship (Fig. DR2A). No direct relationship between the stratabound ore and country rocks was observed at Xinqiao. The colloform pyrite (py2) also contains carbonate veins ($< 1\text{mm} - 1\text{cm}$, Figs. 2B, DR2A and DR2C), but according to the sharp contact relationship between py1 and py2, a recrystallization origin of py1 from py2 is unlikely.

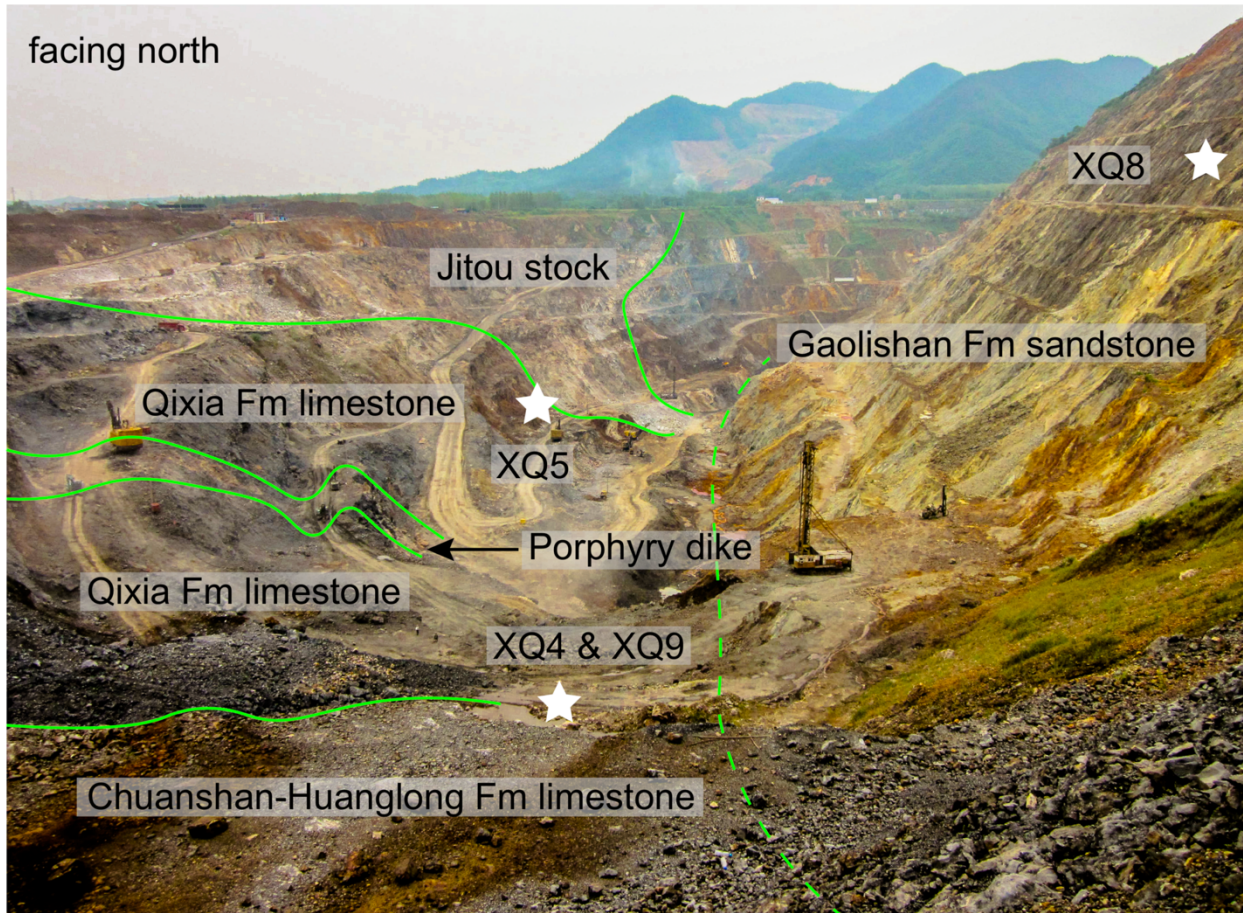


Figure DR1. A photo image of the open pit of Xinqiao, with highlighted deposit geology and sample locations.

The euhedral pyrite ore predominately comprises euhedral to sub-euhedral pyrite (<0.5 to several cm in size, Fig. 2A, DR2B) with a volume percentage of ~80%, the cements are calcite (15%) and quartz (<5%). Pyrite veins (XQ15-5, py3) hosted by the garnet-bearing skarn ore was collected from the northwest wall of the open pit where the Jitou stock intrudes limestone of Permian Qixia Formation (Fig. DR1). The sample predominately contains brown-red garnet grains (<1 cm in size), and is crosscut by pyrite veins, which in turn have been crosscut by quartz veins (Fig. 2C, DR2D). The skarn-pyrite vein (~0.5 cm width) contains sub-euhedral pyrite grains (<1 cm in size). Pyrite veins (XQ15-8, py4) beneath the stratabound orebody were collected from the southeast wall of the open pit (Fig. DR1). The veins are of variable width (<1 cm and >15 cm) and are hosted by sandstone of Carboniferous Gaolishan Formation (Fig. DR2E). The sandstone is

intensively fractured, and extensively silicified. The pyrite grains generally are euhedral, with grain sizes of 0.2 cm to 1 cm, and show open space filling features (Fig. 2D, DR2F). With the exception of silicification and sericitization, no other alteration type is observed or is documented.

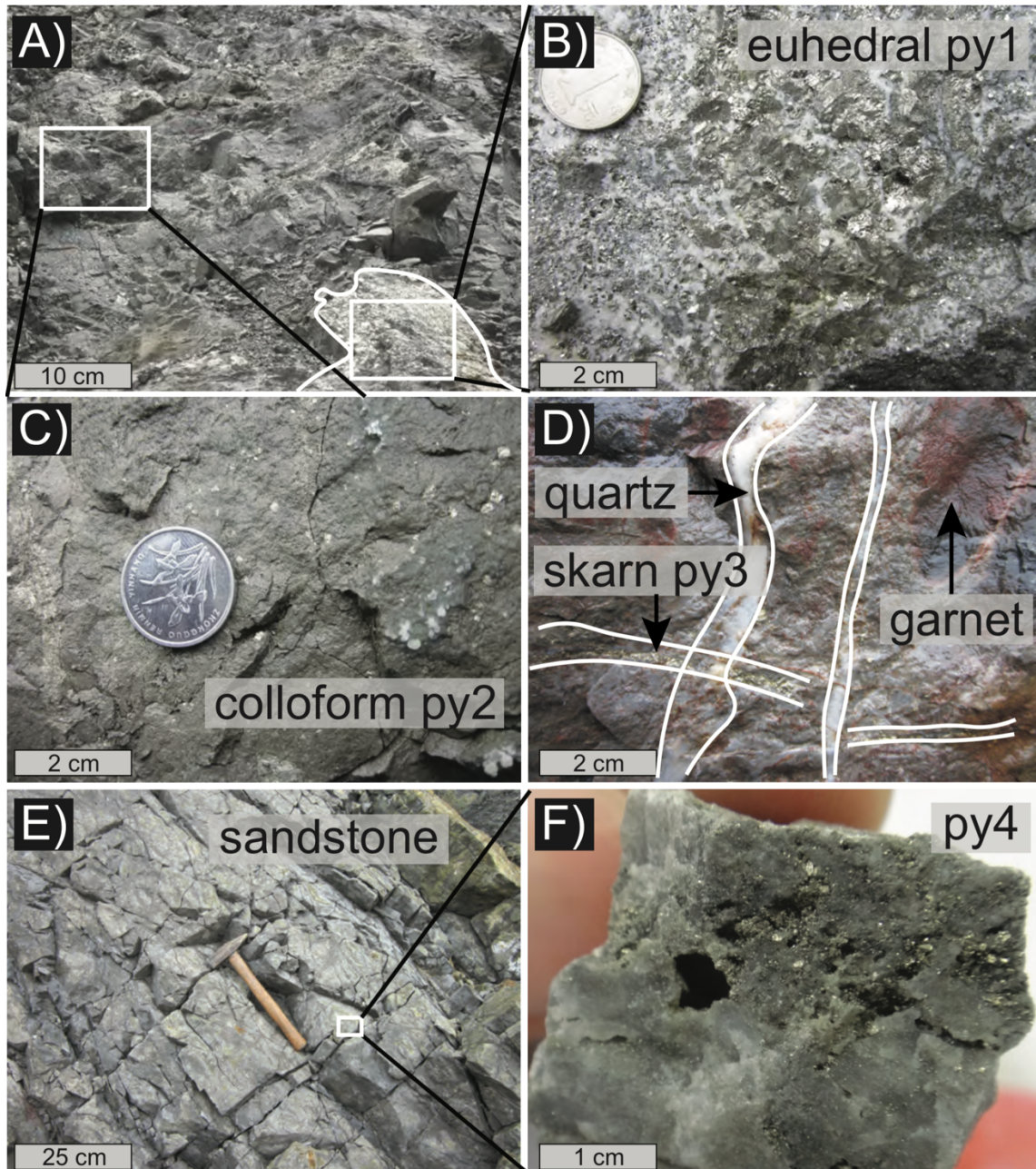


Figure DR2. Samples utilized in this study. A), The sharp contact relationship between the colloform pyrite and euhedral pyrite ores from the stratabound orebody; B), Euhedral pyrite ore (py1); C), Colloform pyrite ore (py2); D), Garnet bearing skarn ore crosscut by quartz and pyrite veins (py3); E), Pyrite veins hosted by Gaolishan Formation sandstone; F), Pyrite-quartz veins (py4) hosted by sandstone show open space filling features.

In most cases, no direct contact relationship is documented/observed between the colloform ore and sedimentary rocks, but colloform pyrite veins cross cuts the Permian limestone are observed locally (Fig. DR3). Beneath the stratabound ore bodies are vertical to sub-vertical Au-bearing pyrite stockworks hosted by the Early Carboniferous Gaolishan Formation sandstone (Guo et al., 2011; Zhang et al., 2017).

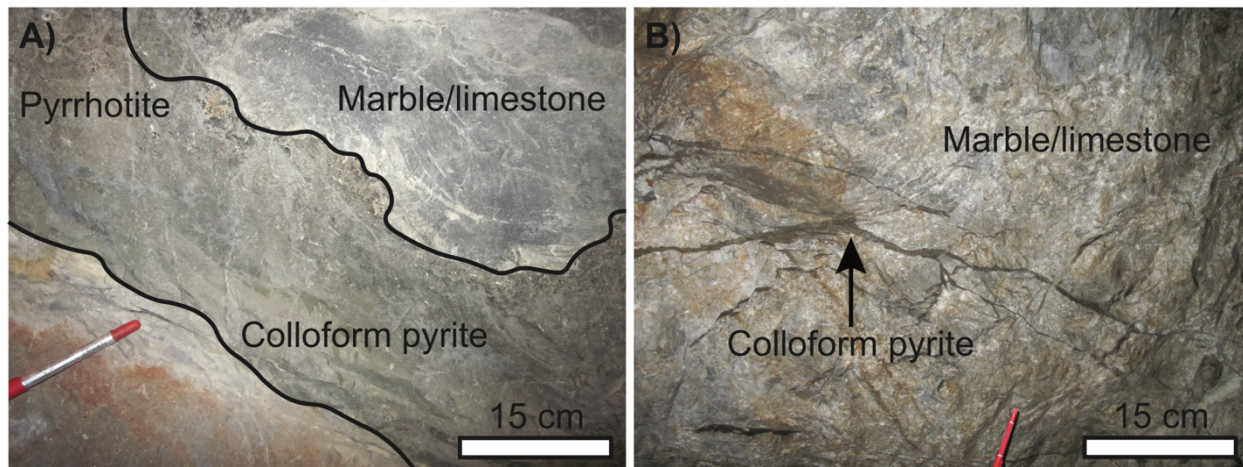


Figure DR3. Colloform pyrite ores cross-cutting Permian marble/limestone at the Dongguashan deposit (A) and the Wushan deposit (B).

A2. Pyrite Re-Os isotope analytical method

After petrographic examination, pyrite-bearing samples were crushed to 20-30 mesh and handpicked under a microscope; estimated pyrite purity is better than 98 %. The purified pyrite samples were mounted in epoxy resin for further petrographic examination (Fig. 2A) with an aim to document the texture and association with alteration assemblages. The pyrite Re-Os analytical method utilized is the same as previously documented (Selby et al., 2009; Li, et al., 2017) and is briefly outlined here. Purified pyrite aliquots were accurately weighted and loaded into a Carius tube with known amounts of a mixed Re-Os tracer solution containing ^{185}Re and ^{190}Os . The bottom part of the Carius tube was frozen in a mixture of ethanol and dry ice, and 11.5 N HCl (3 ml) and 15.5 N HNO₃ (8 ml) were added. The Carius tube was sealed from the top by a hydrogen-oxygen

torch and then kept in a steel jacket. Sample digestion and sample-spike equilibrium was achieved in an oven at 220 °C for 48 hours. Once cooled, the outside of the Carius tube was rinsed with MQ. The bottom part was frozen again in ethanol-dry ice slurry before being opened from the top by a hydrogen-oxygen torch. Osmium was isolated from the acidic digestion medium using solvent (CHCl_3 *3 times) extraction, and then was back extracted by HBr, and finally purified through microdistillation. Rhenium was separated by solvent extraction (NaOH-acetone) from the acidic medium and then was further purified via anion exchange chromatography. The purified Re and Os were loaded onto Ni and Pt filaments, respectively, and the isotopic measurements were conducted using negative thermal ionization mass spectrometry on a Thermo Electron[®] TRITON mass spectrometer (Creaser et al. 1991; Völkening et al. 1991) at Durham University. The Os data was collected via a secondary electron multiplier in peak-hopping mode, and Re data was collected with static Faraday collectors. Total procedural blanks were monitored over the course of study. Blanks for Re and Os were 2.6 ± 0.4 and 1.5 ± 1.6 pg, respectively, with an average $^{187}\text{Os}/^{188}\text{Os}$ value of 0.21 ± 0.10 (2σ , $n = 5$). For the samples of this study, the presented uncertainties are fully propagated to include uncertainties in Re and Os isotopic compositions measurements, blank abundances and isotopic compositions, spike calibrations and the reproducibility of Re and Os standards. The Re-Os isochron graphs were plotted using Isoplot v4.15 program (Ludwig 2003), with the ^{187}Re decay constant of ^{187}Re of $1.666 \times 10^{-11} \text{a}^{-1}$ (Shirey and Walker 1998; Selby et al. 2007). For pyrite samples hosted by sandstone of Gaolishan Formation, given the extremely low to absence of common Os detected, in addition to using the $^{185}\text{Re} + ^{190}\text{Os}$ enriched spike, we also run duplicated analyses using an $^{185}\text{Re} + \text{normal Os}$ spike as used for molybdenite analysis (Selby and Creaser 2001; Li et al. 2017b). For the same sample, the two methods yield similar data, however, they do not overlap within analytical uncertainty (Table DR1). This indicates that Re-Os

systematics of py4 are not homogeneous, as further supported by their element budgets (Table DR2). Nevertheless, the Re abundances and model dates of py4 from both analytical methods fall on the same trend (Fig. 2F, see main text discussion).

A3. Re-Os data and initial $^{187}\text{Os}/^{188}\text{Os}$ values

For py1, py2 and py3, their initial $^{187}\text{Os}/^{188}\text{Os}$ values are determined through isochron regression of the $^{187}\text{Re}/^{188}\text{Os}$ and $^{187}\text{Os}/^{188}\text{Os}$ data (Fig. 2B), and also recalculated at 138.5 Ma in Table DR1. The two approaches yield indistinguishable results within uncertainties. For py4, the $^{187}\text{Re}/^{188}\text{Os}$ and $^{187}\text{Os}/^{188}\text{Os}$ values are highly radiogenic (70930-170383 and 265-943; Table DR1) and imply that the bulk of the Os is ^{187}Os . The Re-Os isotope data of py4 do not yield any meaningful Re-Os isotopic data and thus their initial $^{187}\text{Os}/^{188}\text{Os}$ value is not known. In this case, an initial $^{187}\text{Os}/^{188}\text{Os}$ value must be assumed in order to calculate the best estimate for the percentage of radiogenic Os, and thus to yield an accurate and precise Re-Os model age. For the py4 sample set, owing to their exceptionally high rhenium abundances and high percentage of radiogenic Os, the overall accuracy of the percentage of radiogenic ^{187}Os (>99.55%), and hence the model age, is relatively insensitive to the assumed initial $^{187}\text{Os}/^{188}\text{Os}$ values (Table DR2).

In order to put tight constraints on the genesis of py4, we further investigate the two proposed genetic scenarios as follows. If we consider py4 are Carboniferous in age (i.e., 320 Ma), then the initial $^{187}\text{Os}/^{188}\text{Os}$ values of these samples would need to be highly variable (-223 and 59), but the presence of both positive and negative values is a geological unlikely scenario. A Cretaceous age (i.e., 138.5 Ma) would also require the sample set to possess highly variable initial $^{187}\text{Os}/^{188}\text{Os}$ values (54 to 549). But the initial $^{187}\text{Os}/^{188}\text{Os}$ values are geologically possible, which could be generated through the interaction with ^{187}Os -rich phases (e.g., molybdenite; see main text for discussion). Such a hypothesis is further supported by the correlation between the Re-Os model

ages, rhenium abundances and Co + Ni + Ag + Ba + Au + Tl values (Figs. 2F and 3C; see main text for discussion), suggesting that a higher degree of interaction with Re- and ¹⁸⁷Os-rich phases resulted in the inheritance of more Re, ¹⁸⁷Os and trace elements. To summarize, we consider a Carboniferous age is unlikely for py4, and instead propose that a Cretaceous age is the most plausible scenario, which is in accordance with the Re-Os age constraints of py1, py2, py3 and geological observations.

A4. Pyrite trace element analytical method

Trace-element abundances were determined using a modification of the procedure of Ottley et al., (2003). Pyrite grains (~100 mg) were digested in 6ml inverse aqua-regia (2:1 mix of 15.5N HNO₃ and 11.5N HCl) in Teflon beakers at 220 °C for 24 h and then evaporated to dryness at 80 °C. At this stage, 1 ml 16N HNO₃ was added and evaporated to near dryness. This process was repeated for three times, and followed by the addition of 10 ml 4N HNO₃. The sample was capped and heated overnight at 100 °C. Once cooled, the solution was transferred to a 50ml centrifuge tube and brought up to 50 ml MQ H₂O. A 1:10 dilution of the sample solution was made prior to sample analysis. Trace elements were analyzed using the Thermo[®] XSERIES 2 mass spectrometer at Durham University. In-house and international reference materials (W-2, BHVO-1, AGV1) were used for calibration and multiple blank analysis were included for each sample set. Reproducibility of elemental runs is estimated to be better than 5% (2 SD).

A5. List of tables and figures

Table DR1. Synopsis of the Pyrite Re-Os data from the Xinqiao deposit.

Table DR2. Synopsis of the pyrite trace element data from the Xinqiao deposit.

Figure DR3. Colloform pyrite ores intruded into Permian marble/limestone at Dongguashan deposit (A) and Wushan deposit (B).

Figure DR2. A photo image of the open pit of Xinqiao, with highlighted deposit geology and sample locations.

Figure DR2. Samples utilized in this study. A), The sharp contact relationship between the colloform pyrite and euhedral pyrite ores from the stratabound orebody; B), Euhedral pyrite ore (py1); C), Colloform pyrite ore (py2); D), Garnet bearing skarn ore crosscut by quartz and pyrite veins (py3); E), Pyrite veins hosted by Gaolishan Formation sandstone; F), Pyrite-quartz veins (py4) hosted by sandstone show open space filling features.

References

- Creaser RA, Papanastassiou DA, Wasserburg GJ (1991) Negative Thermal Ion Mass-Spectrometry of Osmium, Rhenium, and Iridium. *Geochim Cosmochim Acta* 55:397–401. doi: Doi 10.1016/0016-7037(91)90427-7
- Guo, W.M., Lu, J.J., Jiang, S.Y., Zhang, R.Q., and Qi, L., 2011, Re-Os isotope dating of pyrite from the footwall mineralization zone of the Xinqiao deposit, Tongling, Anhui Province: Geochronological evidence for submarine exhalative sedimentation: *Chinese Science Bulletin*, v. 56, p. 3860–3865, <https://doi.org/10.1007/s11434-011-4770-y>.
- Li Y, Li JW, Li XH, et al (2017a) An Early Cretaceous carbonate replacement origin for the Xinqiao stratabound massive sulfide deposit, Middle-Lower Yangtze Metallogenic Belt, China. *Ore Geol Rev* 80:985–1003. doi: 10.1016/j.oregeorev.2016.08.017
- Li Y, Selby D, Condon D, Tapster S (2017b) Cyclic magmatic-hydrothermal evolution in porphyry systems: High-precision U-Pb and Re-Os geochronology constraints from the Tibetan Qulong porphyry Cu-Mo deposit. *Econ Geol* 112:1419–1440. doi: 10.5382/econgeo.2017.4515
- Ludwig KR (2003) User's manual for Isoplot 3.00: a geochronological toolkit for Microsoft Excel. Kenneth R. Ludwig
- Ottley CJ, Pearson DG, Irvine GJ (2003) A Routine Method for the Dissolution of Geological Samples for the Analyses of REE and Trace Elements Via ICP-MS. *Plasma Source Mass Spectrom Appl Emerg Technol* 221–230. doi: 10.1039/9781847551689-00221
- Selby D, Creaser RA (2001) Re-Os geochronology and systematics in molybdenite from the Endako porphyry molybdenum deposit, British Columbia, Canada. *Econ Geol* 96:197–204. doi: Doi 10.2113/96.1.197

- Selby D, Creaser RA, Stein HJ, et al (2007) Assessment of the ^{187}Re decay constant by cross calibration of Re–Os molybdenite and U–Pb zircon chronometers in magmatic ore systems. *Geochim Cosmochim Acta* 71:1999–2013. doi: 10.1016/j.gca.2007.01.008
- Selby D, Kelley KD, Hitzman MW, Zieg J (2009) Re–Os sulfide (bornite, chalcopyrite, and pyrite) systematics of the carbonate-hosted copper deposits at Ruby Creek, Southern Brooks Range, Alaska. *Econ Geol* 104:437–444.
- Shirey SB, Walker RJ (1998) The Re–Os isotope system in cosmochemistry and high-temperature geochemistry. *Annu Rev Earth Planet Sci* 26:423–500. doi: DOI 10.1146/annurev.earth.26.1.423
- Völkening J, Walczyk T, Heumann KG (1991) Osmium isotope ratio determinations by negative thermal ionization mass spectrometry. *Int J Mass Spectrom Ion Process* 105:147–159.
- Xu, G., and Zhou, J., 2001, The Xinqiao Cu–S–Fe–Au deposit in the Tongling mineral district, China: Synorogenic remobilization of a stratiform sulfide deposit: *Ore Geology Reviews*, v. 18, p. 77–94, [https://doi.org/10.1016/S0169-1368\(01\)00017-8](https://doi.org/10.1016/S0169-1368(01)00017-8).
- Zhang, Y., Shao, Y.J., Li, H.B., and Liu, Z.F., 2017, Genesis of the Xinqiao Cu–S–Fe–Au deposit in the Middle-Lower Yangtze River Valley metallogenic belt, Eastern China: Constraints from U–Pb–Hf, Rb–Sr, S, and Pb isotopes: *Ore Geology Reviews*, v. 86, p. 100–116, <https://doi.org/10.1016/j.oregeorev.2017.02.014>.

Table DR1, Pyrite Re-Os data from Xinqiao deposit

Sample	Weight (g)	Re (ppb)	2σ	Os (ppt)	2σ	¹⁹² Os (ppt)	2σ	¹⁸⁷ Re/ ¹⁸⁸ Os	2σ	¹⁸⁷ Os/ ¹⁸⁸ Os	2σ	rho	% ¹⁸⁷ Osr	Os _i @ 138.5 Ma	2σ
<i>Py1, euhedral pyrite from stratabound orebody</i>															
XQ15-9-1	0.42	1.47	0.01	7.76	0.24	2.18	0.13	1343.42	82.83	3.72	0.27	0.820	76.6	0.63	0.46
XQ15-9-2	0.41	2.58	0.02	14.11	0.27	3.95	0.13	1299.34	42.92	3.75	0.15	0.823	76.8	0.76	0.24
XQ15-9-4	0.43	2.03	0.01	7.32	0.21	1.71	0.10	2367.32	141.74	6.01	0.38	0.929	85.5	0.56	0.71
XQ15-9-5	0.40	1.58	0.02	10.29	0.19	3.06	0.11	1024.68	38.02	3.11	0.12	0.891	72.0	0.75	0.21
XQ15-9-6	0.41	3.59	0.02	12.94	0.25	2.96	0.10	2412.85	84.13	6.29	0.23	0.940	86.2	0.73	0.42
													weighted mean	0.73	0.14
<i>Py2, colloform pyrite from stratabound orebody</i>															
XQ15(coarse)-4-1	0.40	9.28	0.03	68.95	0.74	19.81	0.21	932.11	10.26	3.47	0.05	0.649	65.5	1.33	0.08
XQ15(coarse)-4-2	0.41	5.62	0.02	116.49	0.95	38.25	0.35	292.47	2.88	2.10	0.03	0.670	42.9	1.43	0.03
XQ15(coarse)-4-3	0.45	2.44	0.01	26.12	0.61	8.09	0.29	599.77	21.53	2.67	0.15	0.614	55.1	1.29	0.20
XQ15(coarse)-4-4	0.41	3.22	0.02	45.09	0.55	14.48	0.24	442.86	7.64	2.31	0.05	0.687	48.1	1.29	0.07
XQ15(coarse)-4-5	0.45	6.89	0.02	18.02	0.66	2.88	0.23	4762.58	356.88	12.28	0.99	0.928	90.2	1.32	1.81
XQ15(fine)-4-0	0.40	1.20	0.02	7.37	0.25	2.01	0.14	1184.49	80.40	4.04	0.32	0.819	70.3	1.32	0.51
XQ15(fine)-4-1	0.40	7.64	0.02	56.07	0.62	16.05	0.20	947.50	12.09	3.52	0.06	0.729	65.9	1.34	0.09
XQ15(fine)-4-2	0.43	8.14	0.03	133.26	1.75	43.35	0.57	373.75	5.17	2.19	0.06	0.448	45.2	1.33	0.07
XQ15(fine)-4-3	0.40	2.22	0.02	36.16	0.49	11.76	0.17	375.33	6.10	2.20	0.06	0.441	45.4	1.33	0.08
XQ15(fine)-4-4	0.41	3.93	0.02	51.21	0.51	16.31	0.19	478.98	6.02	2.40	0.04	0.657	50.0	1.30	0.05
XQ15(fine)-4-5	0.41	5.47	0.03	38.80	0.67	11.02	0.24	987.86	21.49	3.61	0.12	0.625	66.7	1.33	0.17
													weighted mean	1.36	0.02
<i>Py3, euhedral pyrite from garnet bearing skarn ore</i>															
XQ15-5-3	0.41	1.55	0.02	7.66	0.42	2.07	0.31	1490.23	73.57	4.18	0.21	0.961	71.3	0.74	0.27
XQ15-5-4	0.40	1.35	0.02	5.67	0.41	1.41	0.31	1904.13	137.40	5.16	0.38	0.980	69.8	0.77	0.49
													weighted mean	0.74	0.24

Py4, euhedral pyrite from the quartz-pyrite stockworks hosted by Gaolishan Formation sandstone

Name	Re (ppb)	2σ	Os (ppt)	2σ	¹⁹² Os (ppt)	2σ	¹⁸⁷ Re/ ¹⁸⁸ Os	2σ	¹⁸⁷ Os/ ¹⁸⁸ Os	2σ	rho	¹⁸⁷ Re (ppb)	2σ	¹⁸⁷ Os (ppt) ¹	2σ	% ¹⁸⁷ Osr ¹	Age	2σ	Os _i for 138.5 Ma	2σ	Os _i for 320 Ma	2σ
XQ15-8-1	0.10	3692.22	11.19	12902.16	230.79	43.11	0.81	170382.78	3252.10	942.81	18.42	0.953	2320.69	7.03	12825.12	66.36	99.87	330.8	1.7	549.2	32.0	
XQ15-8-2	0.10	525.56	1.59	1615.55	54.30	10.54	0.78	99163.29	7351.46	480.52	35.66	0.997	330.33	1.00	1596.71	7.45	99.75	289.4	1.3	251.4	-49.5	
XQ15-8-3	0.20	267.88	0.80	1020.06	32.32	6.02	0.39	88465.51	5778.02	531.51	34.78	0.996	168.37	0.50	1010.06	5.14	99.85	359.0	1.8	327.1	58.6	
XQ15-8-4	0.30	124.95	0.37	367.80	12.53	3.50	0.27	70929.58	5410.18	327.72	25.03	0.997	78.54	0.23	361.54	1.91	99.63	275.7	1.5	163.9	-51.4	
XQ15-8-5	0.20	366.51	1.09	1359.73	36.10	8.84	0.40	82464.29	3754.56	482.29	22.03	0.992	230.37	0.69	1343.93	6.50	99.75	349.2	1.7	291.8	41.5	
XQ15-8-6	0.41	71.81	0.21	182.67	8.55	1.37	0.20	104594.60	15084.31	418.85	60.45	0.999	45.14	0.13	180.40	1.14	99.81	239.4	1.5	177.2	-140.3	
XQ15-8-7	0.30	57.79	0.17	107.23	6.08	1.26	0.27	91223.10	19240.35	264.84	55.91	0.999	36.32	0.11	104.98	1.01	99.55	173.2	1.7	54.1	-222.8	

1, Abundances and percentage of radiogenic ¹⁸⁷Os are estimated with an initial ¹⁸⁷Os/¹⁸⁸Os value of 1.2, see main text and DR for discussions.

Py4, euhedral pyrite from the quartz-pyrite stockworks hosted by Gaolishan Formation sandstone, re-analysed using a spike enriched in ¹⁸⁵Re with a normal Os composition as used for molybdenite

Sample	wt	Re(ppb)	2σ	¹⁸⁷ Re(ppb)	2σ	¹⁸⁷ Os(ppt)	2σ	Age	2σ
XQ15-8-1	0.15	2172.54	7.32	1365.48	4.60	8641.73	23.47	378.7	1.6
XQ15-8-5	0.25	346.61	2.46	217.85	1.55	1296.32	8.85	356.1	3.5
XQ15-8-6	0.44	75.34	1.53	47.35	0.96	187.66	3.78	237.4	6.8
XQ15-8-7	0.16	59.32	2.97	37.29	1.87	120.07	6.01	193.0	13.7

Common Os cannot be detected with S/N spike.

Table DR2, Pyrite trace elements data from Xinqiao deposit

	weight/g	Mn ppm	Sb ppm	Cu ppm	Pb ppm	Zn ppm	Mo ppm	W ppm	Ag ppm	Au ppm	Ba ppm	Co ppm	Ni ppm	Tl ppm	Co+Ni+Ag+Ba+Au+Tl ppm	Cu+Zn+Mo+W+Pb ppm	ppb	Re Ma	Age
<i>Py1, euhedral pyrite from stratabound orebody</i>																			
XQ15-9-1	0.1	2466.1	0.0	155.5	8.3	10.7	0.0	36.7	4.1	0.0	0.0	0.0	0.0	0.0	0.0	4.2	211.2	1.5	135.3
XQ15-9-2	0.1	1329.7	0.0	111.4	3.6	6.9	0.0	18.2	0.9	0.0	0.0	0.0	0.0	0.0	0.0	0.9	140.0	2.6	135.3
XQ15-9-4	0.1	2817.3	0.0	555.4	6.7	4.9	0.0	12.3	0.9	0.0	0.0	0.0	0.0	0.0	0.0	0.9	579.3	2.0	135.3
XQ15-9-5	0.1	2678.3	0.0	407.9	6.4	6.5	0.0	34.5	1.0	0.0	0.0	0.0	0.0	0.0	0.0	1.0	455.4	1.6	135.3
XQ15-9-6	0.1	2814.8	0.0	52.2	7.7	16.4	0.0	40.6	1.0	0.0	0.0	0.0	0.0	0.0	0.0	1.1	116.8	3.6	135.3
<i>Py2, colloform pyrite from stratabound orebody</i>																			
XQ15(fine)-4-0	0.1	5318.4	110.7	769.3	1249.6	190.0	25.7	0.0	27.3	0.0	0.0	0.0	0.0	0.0	0.0	53.0	2234.6	1.2	137.0
XQ15(fine)-4-1	0.1	498.2	137.1	648.0	1054.8	11.0	19.9	0.0	25.8	0.0	0.0	0.0	0.0	0.0	0.0	45.7	1733.7	7.6	137.0
XQ15(fine)-4-2	0.1	2299.2	193.6	981.2	1601.8	20.9	42.5	0.0	30.6	0.0	0.0	0.0	0.0	0.0	0.0	73.2	2646.5	8.1	137.0
XQ15(fine)-4-3	0.1	835.5	124.4	552.2	1077.8	5.1	14.6	0.0	16.5	0.0	0.0	0.0	0.0	0.0	0.0	31.1	1649.6	2.2	137.0
XQ15(fine)-4-4	0.1	2967.5	153.8	1549.3	1193.0	25.4	31.8	0.0	28.0	0.0	0.0	0.0	0.0	0.0	0.0	59.8	2799.5	3.9	137.0
XQ15(fine)-4-5	0.1	148.4	0.6	753.2	129.7	7.4	7.3	0.0	5.6	0.0	0.0	0.0	0.0	0.0	0.0	13.0	897.6	5.5	137.0
XQ15(coarse)-4-1	0.1	632.7	139.9	724.4	1100.6	30.8	20.2	0.0	25.5	0.0	0.0	0.0	0.0	0.0	0.0	45.7	1876.0	9.3	137.0
XQ15(coarse)-4-2	0.1	2200.9	181.0	984.2	1642.7	16.1	35.5	0.0	29.4	0.0	0.0	0.0	0.0	0.0	0.0	64.9	2678.5	5.6	137.0
XQ15(coarse)-4-3	0.1	1070.7	118.4	581.2	1107.0	6.8	15.4	0.0	15.9	0.0	0.0	0.0	0.0	0.0	0.0	31.3	1710.5	2.4	137.0
XQ15(coarse)-4-4	0.1	2045.6	140.0	748.1	1043.5	16.5	24.7	0.0	22.0	0.0	0.0	0.0	0.0	0.0	0.0	46.7	1832.8	3.2	137.0
XQ15(coarse)-4-5	0.1	139.5	0.6	555.9	159.5	4.8	0.4	0.0	7.0	0.0	0.0	0.0	0.0	0.0	0.0	7.4	720.7	6.9	137.0
<i>Py3, euhedral pyrite from garnet bearing skarn ore</i>																			
XQ15-5-3	0.1	1897.4	0.0	11.1	7.3	18.9	0.0	44.9	0.9	0.0	0.0	0.0	0.0	0.0	0.0	0.9	82.2	1.6	138.0
XQ15-5-4	0.1	1625.0	0.0	22.4	3.7	12.0	0.0	20.6	1.0	0.0	0.0	0.0	0.0	0.0	0.0	1.0	58.7	1.4	138.0
<i>Py4, euhedral pyrite from the quartz-pyrite stockworks hosted by Gaolishan Formation sandstone</i>																			
XQ15-8-1	0.1	83.5	60.3	185.8	458.2	95.8	0.0	0.0	17.1	0.3	36.4	76.2	101.0	135.9	290.7	739.8	3692.2	378.7	
XQ15-8-2	0.1	42.0	43.9	155.4	422.4	31.6	0.0	0.0	16.1	0.4	81.0	76.5	79.1	67.5	244.1	609.3	525.6	289.4	
XQ15-8-3	0.1	95.3	54.9	217.4	414.2	61.9	0.0	0.0	27.9	0.1	12.2	35.1	68.2	164.0	272.3	693.5	267.9	359.0	
XQ15-8-4	0.1	37.6	13.8	281.8	182.5	14.3	0.0	0.0	5.8	0.6	28.3	203.5	193.2	8.5	236.4	478.7	125.0	275.7	
XQ15-8-5	0.1	73.3	44.3	209.4	396.0	74.2	0.0	0.0	22.8	0.1	69.4	63.6	96.2	102.4	290.9	679.7	366.5	356.1	
XQ15-8-6	0.1	18.6	17.7	230.1	233.6	34.6	0.0	0.0	5.1	0.3	7.9	62.6	93.8	34.2	141.3	498.3	71.8	239.4	